AIAA JOURNAL
Vol. 32, No. 1, January 1994

Head-On Parallel Blade-Vortex Interaction

Soogab Lee* and Daniel Bershader†
Stanford University, Stanford, California 94305

An experimental and computational study was carried out to investigate the parallel head-on blade-vortex interaction (BVI) and its noise generation mechanism. A shock tube, with an enlarged test section, was used to generate a compressible starting vortex which interacted with a target airfoil. The dual-pulsed holographic interferometry (DPHI) technique and airfoil surface pressure measurements were employed to obtain quantitative flowfield data during the BVI. A thin-layer Navier-Stokes code (BVI2D), with a high-order upwind-biased scheme and a multizonal grid, was also used to simulate numerically the phenomena occurring in the head-on BVI. The detailed structure of a convecting vortex was studied through independent measurements of density and pressure distributions across the vortex center. Results indicate that, in a strong head-on BVI, the opposite pressure peaks are generated on both sides of the leading edge as the vortex approaches. Then, as soon as the vortex passes by the leading edge, the high-pressure peak suddenly moves toward the low-pressure peak—reducing in magnitude as it moves—simultaneously giving rise to the initial sound wave. In both experiment and computation, it is shown that the viscous effect plays a significant role in head-on BVIs.

Introduction

ROTOR impulsive noise is, of all the known sources of helicopter far-field noise radiation, the one which dominates the acoustic spectrum of most helicopters. The helicopter generates a highly directional and rather unique form of impulsive noise which is thought to be generated by two source mechanisms; these are 1) high-speed impulsive noise due to the formation of a shock on the advancing blade tip, and 2) blade-vortex interaction (BVI) in descending flight or maneuvers, especially during an approach to a landing (Fig. 1). These sources are distinct, unrelated, and complex phenomena. Particularly, in the case of BVI noise, the noise-generating mechanism depends strongly on the local aerodynamic state of the rotor blade, thereby making the theoretical calculations difficult to compare with the experiments.

Schmitz and Boxwell[1] found, from their full-scale in-flight experiments, that the BVI acoustic signal propagates mostly forward and below the rotor tip-path plane, whereas high-speed impulsive noise propagates mainly forward of the rotor tip-path plane. They also reported acoustic far-field impulsive noise patterns for a wide range of steady operating conditions. Tangler[2] investigated the mechanism of helicopter noise through schlieren flow visualization, aided by full-scale blade pressure measurements in the wind tunnel, and found that shock waves play a role in many of the BVIs. Nakamura[3] performed the calculation of the acoustic far field using the experimental data obtained on the operational loads survey (OSL) blade, based on the assumption that only unsteady surface-pressure variations contribute to the radiated noise. However, that study was of limited success since the experimental data did not contain sufficient pressure information required for the prediction. Recently, Caradonna et al.[4] carried out airfoil surface-pressure measurements during BVI at Mach numbers ranging from subsonic to transonic levels and found that significant BVI phenomena were concentrated near the leading edge with a rapid decrease in magnitude toward the trailing edge. They also reported that the qualitative effect of proximity (miss distance) on close BVIs is not great, even for head-on interactions, even though proximity is the strongest factor on the magnitude of pressure pulse. This led them to conclude that a detailed viscous modeling is not required for predicting the BVI on the advancing side (the case of a negative vortex toward the airfoil). Straus et al.[5] also measured airfoil surface-pressure variations during parallel BVI (including near head-on cases). They reported that some cases of BVI can produce a large separation which the airfoil does not recover from until the vortex is well past the trailing edge. This caused them to conclude that a proper viscous model would be required for blade-vortex interaction theory. Meier and Obermeier[6] performed a digital hologram analysis for transonic parallel BVI in both a transonic wind tunnel and a shock tube. They observed viscosity effects, such as flow separation at the leading edge and secondary vortices at the shoulder of the airfoil, similar to those reported by Bershader.[7] But they mentioned that the viscous effect seemed to be of secondary importance only in transonic flow. Booth[8] also reported an evidence of vortex splitting during BVI and concluded the distortion of the vortex core and the vortex trajectory are strongly affected by blade loading.

It is evident that in flight the interaction is made more complex because of three-dimensional distortion and partial

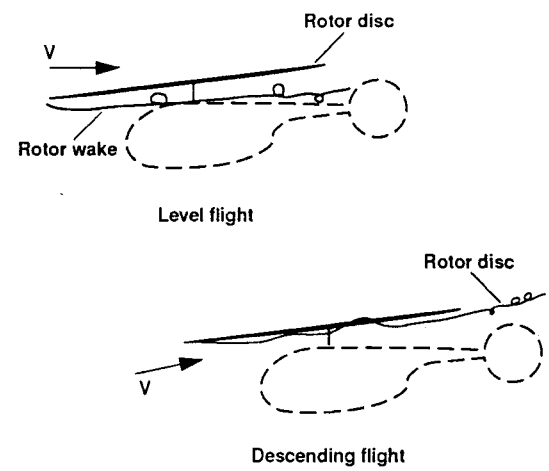

Fig. 1 Interaction of tip vortices with a rotor disk for level and descending flights.

Presented as Paper 91-3277 at the AIAA 9th Applied Aerodynamics Conference, Baltimore, MD, Sept. 23-26, 1991; received March 13, 1992; revision received May 6, 1993; accepted for publication May 12, 1993.

*Research Assistant; currently Research Scientist, Sterling Federal Systems/U.S. Army AFDD, NASA Ames Research Center, Moffett Field, CA 94035. Member AIAA.

†Professor, Department of Aeronautics and Astronautics. Fellow AIAA.

randomization of the vorticity field; therefore, in general, the generic BVI problem (Fig. 2) is unsteady and three dimensional. However, there are two limiting cases that are determined by the intersection angle Λ between the vortex axis and the airfoil span direction. When $\Lambda = 90$ deg (perpendicular interaction), the problem becomes steady and three-dimensional, but when $\Lambda = 0$ deg (parallel interaction), it is unsteady and two dimensional, as can be seen in Fig. 3. Obviously, among parallel interactions, the head-on collisional case affects most strongly the aerodynamics on the leading edge and radiates the strongest sound wave.

The objective of this study is to present the significant results from experiments and computations on the head-on parallel BVI. First, a compressible, viscous vortex was generated in a specially built shock tube and its structure was carefully studied through independent density and pressure measurements. Second, the head-on BVI phenomena were visualized through a holographic interferometry technique, with surface-pressure measurements at selected points. Third, the interferograms and surface-pressure traces were compared with the computed results from a Navier-Stokes equation solver, which has a capability to resolve the distortion or splitting of the convecting vorticity as well as the separation of the boundary layer, both of which can happen in head-on BVIs.

Description of Experiment

A shock tube, which has a rectangular test section, was designed to investigate a two-dimensional BVI problem. The test section allows the shock to diffract essentially cylindrically, as illustrated in Fig. 4; thus, the two-dimensional feature of the flowfield is retained. The diffracted shock is curved; however, the central section which interacts with the vortex generator is closely planar. In this figure, the oblique solid line represents the shock speed, which diminishes as the shock begins to diffract after the area change ($x = 0$ on the horizontal scale). The dotted line which forks off the solid line represents the path of the convected vortex following separation from the generating airfoil. The cross section of the main shock tube is 5×5 cm, with the vertical dimension increasing to 50 cm at $x = 0$. Plexiglas windows, measuring 25×36 cm, were mounted parallel to each other on opposite sides of the test section. The time duration of a quasiuniform flow after a shock passes is about 4 ms. To measure the speed of the shock, two Kulite miniature transducers (diameter 1/32 in.) were employed upstream from the test section. An NACA 0018 airfoil was used as a vortex generator, which had a chord of 3.8 cm and a span of 5 cm. An NACA 0012, which had a chord of 5 cm and a span of 5 cm, was selected as a target airfoil. The freestream Reynolds number, based on the chord of the target airfoil, ranged from 0.9×10^6 to 1.3×10^6.

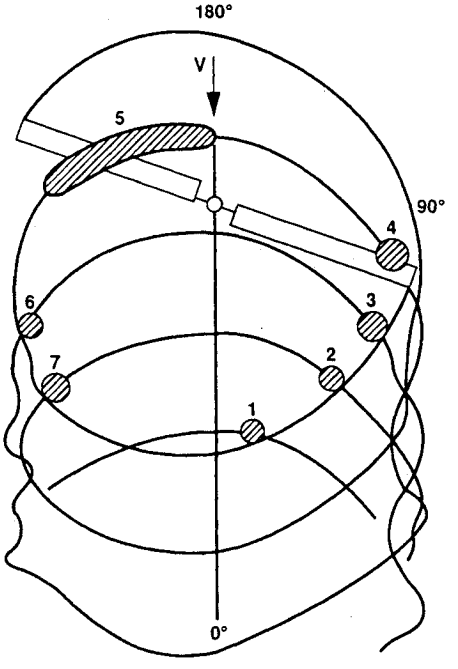

Fig. 2 Blade-vortex interactions during partial-power descent flight (from Tangler[2]).

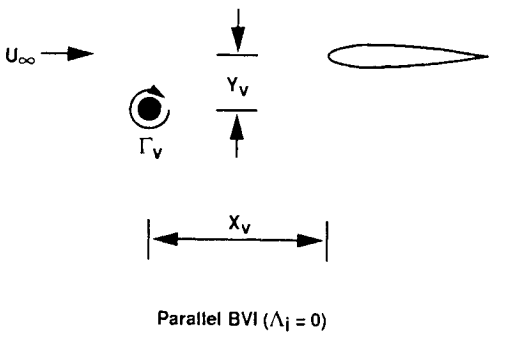

Fig. 3 Typical parallel blade-vortex interaction and its parameters.

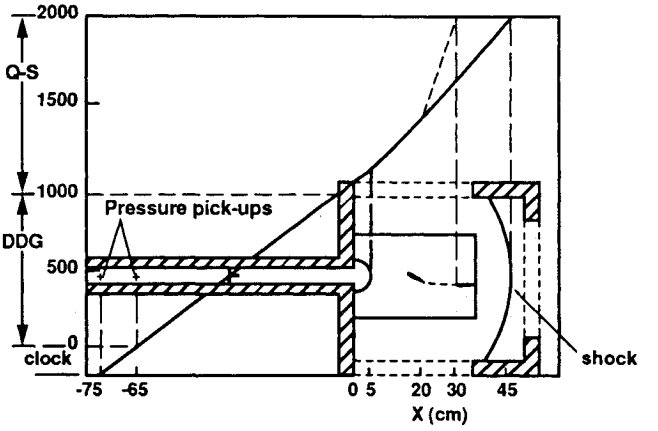

Fig. 4 Schematic diagram of the shock-tube configuration with x-y plot of the shock wave and vortex, superimposed.

A dual-pulsed holographic interferometry (DPHI) technique (Fig. 5) was employed not only to determine the exact trajectory of the convecting vortex, but also to measure the density distribution of the flowfield. For synchronizing the laser light source discharge with the shock motion, the signal from the second pressure transducer was used, after a delay set by a digital delay generator together with the inherent delay in the Q-switch laser pulse mechanism. The time duration of the ruby laser pulse was 10 ns. Agfa Gavart 10E75, which has a resolution of 2800 lines/mm, was used as an emulsion plate. The emulsion plate recorded two holograms in two steps. The first exposure was made when the fluid was at rest, and the second one was made at the time of interest. These exposures produced two different interference patterns due to the phase shift of the second object beam according to the distribution of density of the flow in the test section. These image-plane holograms were reconstructed with the use of a sodium lamp. The fringes in the hologram represent contours of constant density, the increment between fringes corresponding to 0.06 kg/m^3, which is about 1/20 of the atmospheric density, in accordance with the equation

$$S(x, y) - S(x, y)_{\text{ref}} = [KL(\rho - \rho_{\text{ref}})/\lambda_0] \quad (1)$$

where K is the Dale-Gladstone constant, λ_0 the wavelength of pulsed ruby laser, ρ_{ref} the density at a reference point, and L the span of test section. The diaphragm pressure ratio was controlled $\pm$ 1% from shot to shot by standardizing the thick-

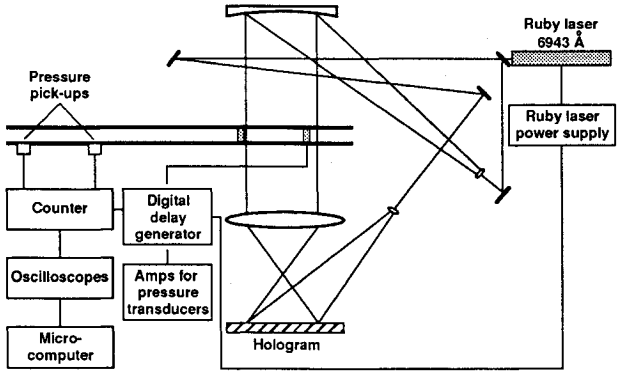

Fig. 5 Schematic top view of the experimental setup for holographic interferometry and airfoil surface pressure measurements.

ness of the polyester (mylar) sheets. After the trajectory was determined, the pressure distributions of the vortex were obtained by use of fast-response miniature pressure gauges, mounted on the surface of the test-section window, which provided time histories across the vortex during its passage. For the trajectory of the vortex center to pass exactly over the surface of the pressure gauge, the position of the pressure transducer was adjusted, after several shots, by rotating its circular holder on which the pressure transducer was embedded eccentrically. It is believed that the freestream flow and the convecting vortex is very close to two dimensional, even though there are boundary layers on the windows of test section, since the fringes recorded by the interferograms are without distortion. From independent measurements of density and pressure distributions across the vortex center, the circumferential velocity distribution of the vortex can be obtained. For an axisymmetric, compressible, viscous flow, and assuming that the center of vortex is convected with the freestream velocity, the radial momentum equation with respect to the vortex center can be expressed as follows:

$$\frac{\partial v_r}{\partial t} + v_r \frac{\partial v_r}{\partial r} + \frac{1}{\rho}\frac{\partial p}{\partial r} - \frac{v_\theta^2}{r} - \frac{2}{\rho}\left(\frac{\partial}{\partial r}\mu\frac{\partial v_r}{\partial r} + \frac{\mu}{r}\frac{\partial v_r}{\partial r} - \frac{\mu v_r}{r^2}\right) = 0 \quad (2)$$

This equation can be simplified by the fact that the radial velocity into the vortex center is much smaller (by at least four orders of magnitudes[7]) than the tangential velocity of the vortex in the two-dimensional flows. Therefore, all terms involving with the radial velocity v_r can be neglected in the radial momentum equation, and the expression reduces to one involving the tangential velocity,

$$\frac{1}{\rho(r)}\frac{\partial p(r)}{\partial r} = \frac{v_\theta(r)^2}{r} \quad (3)$$

To measure the pressure fluctuation on the airfoil during the BVI, miniature pressure transducers, which have a 260 kHz natural frequency, were installed at chordwise locations of 2, 5, and 10% from the leading edge of the target airfoil.

Description of Computation

The unsteady, thin-layer, Navier-Stokes equations were solved for a head-on BVI problem. A fifth-order accurate upwind-biased scheme, based on the Osher-type of flux differencing, was used since it is more effective than conventional second-order central difference or upwind schemes in preserving the structure of the convecting vortex correctly, especially in the case of a head-on collision. The three reasons are 1) the central difference scheme requires the use of artificial viscosity (smoothing parameters) to stabilize it, 2) the Osher scheme better represents the physics of the convection of vorticity because it is formed on the basis of the theory of characteristics, and 3) the stencil size is reduced for same order of accuracy (seven points for upwind biased whereas 11 points for fully upwind). For details about the algorithm, the reader is referred to the works of Rai and Chakravarthy[9] and Rai.[10] The C type of multizone grid surrounding the airfoil was used for this calculation, with the outer boundaries being approximately 10 chords away in every direction from the center of the airfoil. As seen in Fig. 6, zones 1 and 2 are symmetric, whereas zone 3 is a tubelike region that extends from the leading-edge part of the airfoil to the outer boundary. The reason for using this kind of multizone grid is that a high grid density is needed only in zone 3, which is near the path of the vortex, for preserving the vortices. The grids in all three zones were generated by using a combination of algebraic and elliptic grid generation procedures. The grids are orthogonal to the surface of the airfoil. Zones 1 and 2 are discretized with 121 × 151 grids and zone 3 is discretized with a 273 × 573 grid, making a total of approximately 193,000 grid points. At the solid boundaries (lower boundaries of all three grids), the no-slip condition and an adiabatic wall condition are imposed along with an assumption that the derivative of pressure normal to the wall surface is zero. All of these conditions and the equations of state together yield

$$\frac{\partial \rho}{\partial n} = 0 \quad (4)$$

$$\frac{\partial e}{\partial n} = u\frac{\partial \rho u}{\partial n} + v\frac{\partial \rho v}{\partial n} \quad (5)$$

where n is the direction normal to the airfoil surface.

For the far-field boundaries of all three zones, the method of characteristics can be used to specify the conditions. Since the upper boundaries $\eta = \eta_{\max}$ are subsonic inlet boundaries, three quantities need to be specified and one quantity is extrapolated from the interiors of these zones. It is known that, for the unsteady two-dimensional case, there are four characteristics and four Riemann invariants. The first three conditions to be specified are the generalized Riemann invariants given by

$$R_1 = \frac{\eta_t + u\eta_x + v\eta_y}{\sqrt{\eta_x^2 + \eta_y^2}} - \frac{2c}{\gamma - 1}$$
$$R_2 = \frac{v\eta_x - u\eta_y}{\sqrt{\eta_x^2 + \eta_y^2}} \qquad R_3 = \frac{p}{\rho^\gamma} \quad (6)$$

The fourth quantity which is necessary to update the points on this boundary is also a Riemann invariant

$$R_4 = \frac{\eta_t + u\eta_x + v\eta_y}{\sqrt{\eta_x^2 + \eta_y^2}} + \frac{2c}{\gamma - 1} \quad (7)$$

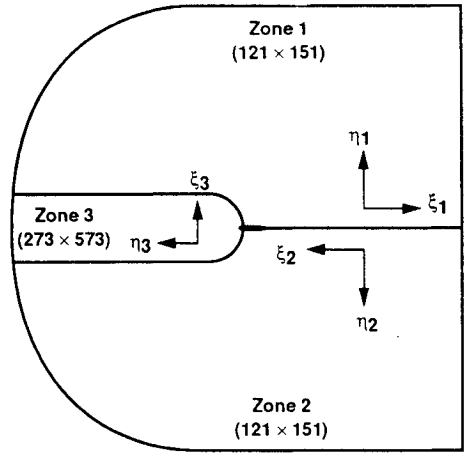

Fig. 6 Computational multizonal, patched grid (193,000 grid points total).

The right boundary of zone 1 and the left boundary of zone 2 are subsonic exit boundaries. A simple, implicit-extrapolation procedure followed by an explicit, postupdate correction is used at these boundaries. The implicit part of the boundary condition for zone 1 is

$$(\tilde{Q}^{p+1}_{i\max,j} - \tilde{Q}^{p}_{i\max,j}) - \frac{J_{i\max-1,j}}{J_{i\max,j}}(\tilde{Q}^{p+1}_{i\max-1,j} - \tilde{Q}^{p}_{i\max-1,j}) = 0 \quad (8)$$

where $\tilde{Q}$ is the solution vector and J is the Jacobian. This step is followed by the explicit correction

$$p_{i\max,j} = p_\infty$$

The freestream pressure (p_∞) is then replaced by the pressure corresponding to the composite vortex in a freestream solution, provided the grid system contains a vortex. The last boundary is the airfoil wake, which separates zones 1 and 2. Although the grid lines of zones 1 and 2 are continuous across the wake, for convienence the wake boundary is also treated as a patch boundary. For the manner in which these boundary conditions can be implemented implicitly and the method for transfering the information in a time-accurate manner across the patch boundaries, see Rai and Chaussee[11] and Rai.[12]

For the analytical structure of the vortex to closely resemble the one measured in the experiments, the maximum circulation, the core radius, and the peak tangential velocity must be identical. A vortex model used by Sculley[13] is expressed as

$$\frac{v_\theta}{U_\infty} = \frac{\hat{\Gamma}}{2\pi r}\left(\frac{r^2}{r^2 + a_0^2}\right) \quad (9)$$

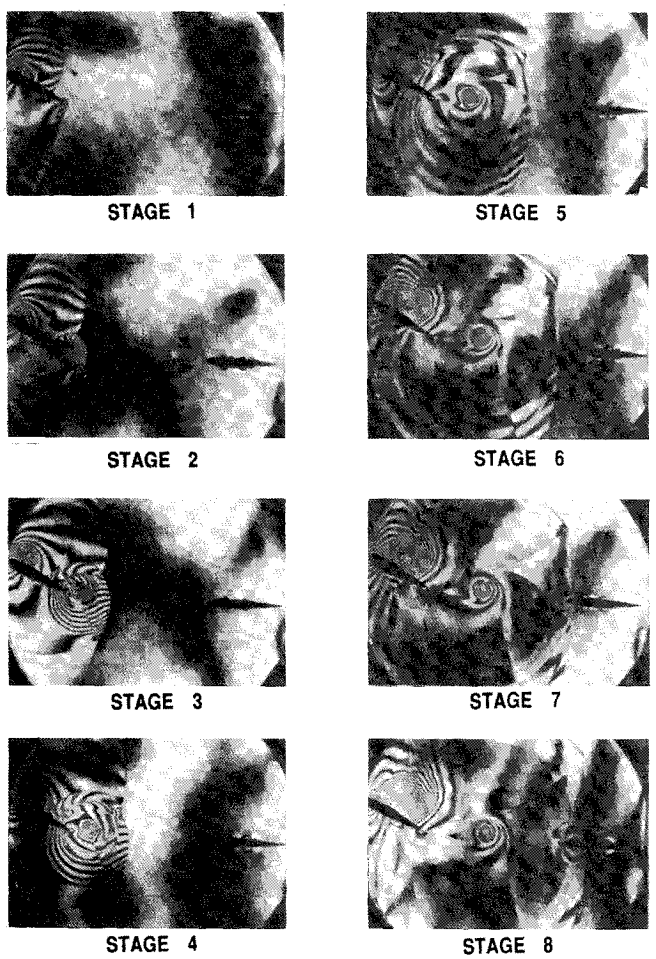

Fig. 7 Eight successive holographic interferograms at 25-μs intervals, showing the generation of a shock-induced starting vortex and the convection to the target airfoil in the test section of the shock tube.

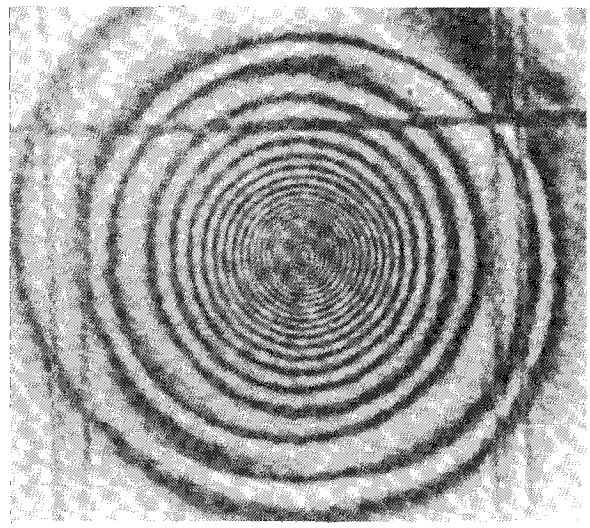

Fig. 8 Holographic interferogram of the vortex.

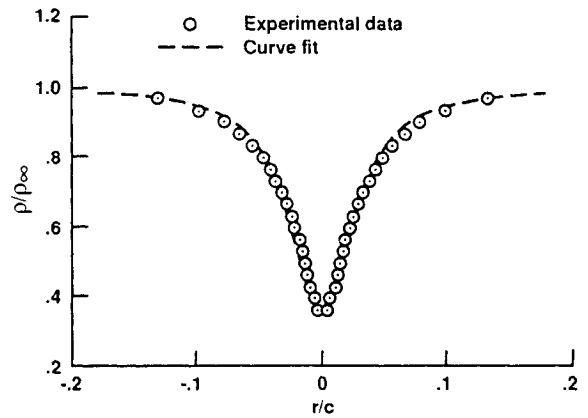

Fig. 9 Measured density profile of the vortex and its curve fit.

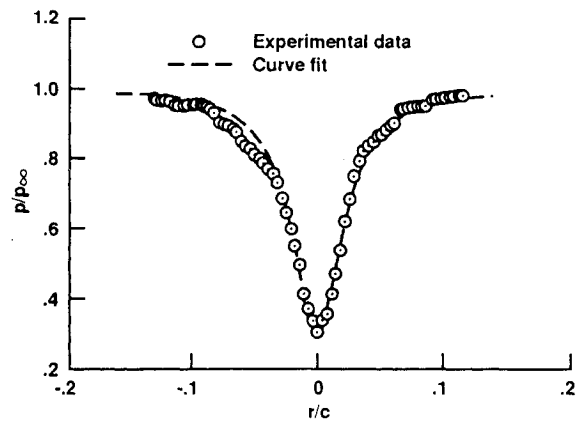

Fig. 10 Measured pressure profile of the vortex and its curve fit.

where a_0 and r are the core radius and the distance from the center of the vortex, respectively, and both are nondimensionalized by the chord length of the airfoil. $\hat{\Gamma}$ is defined by the maximum circulation divided by the freestream velocity and the chord length. The sign of the vortex is defined as negative when the direction of the flow is clockwise. The pressure and density for the vortex convecting in the freestream are related by

$$\frac{dp}{dr} = \frac{\rho v_\theta^2}{r} \quad (10)$$

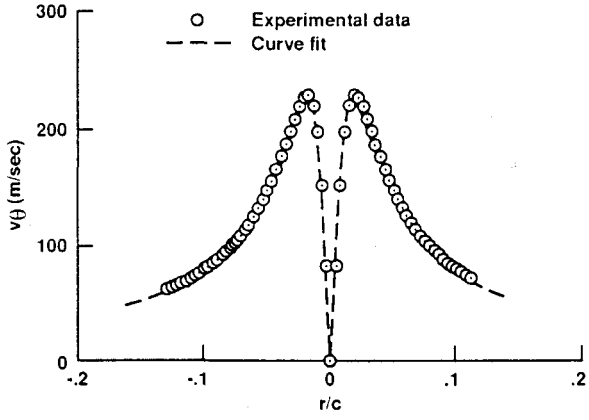

Fig. 11 Velocity profile calculated from measurements of the density and pressure distributions across the vortex and its curve-fit by the analytical model [Eq. (18)].

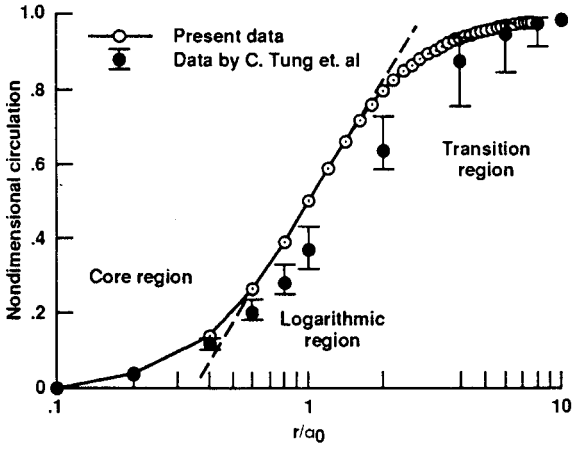

Fig. 12 Semilog plot of the normalized circulation (Γ/Γ_{max}) with respect to the distance from the center of the vortex (r/a_0).

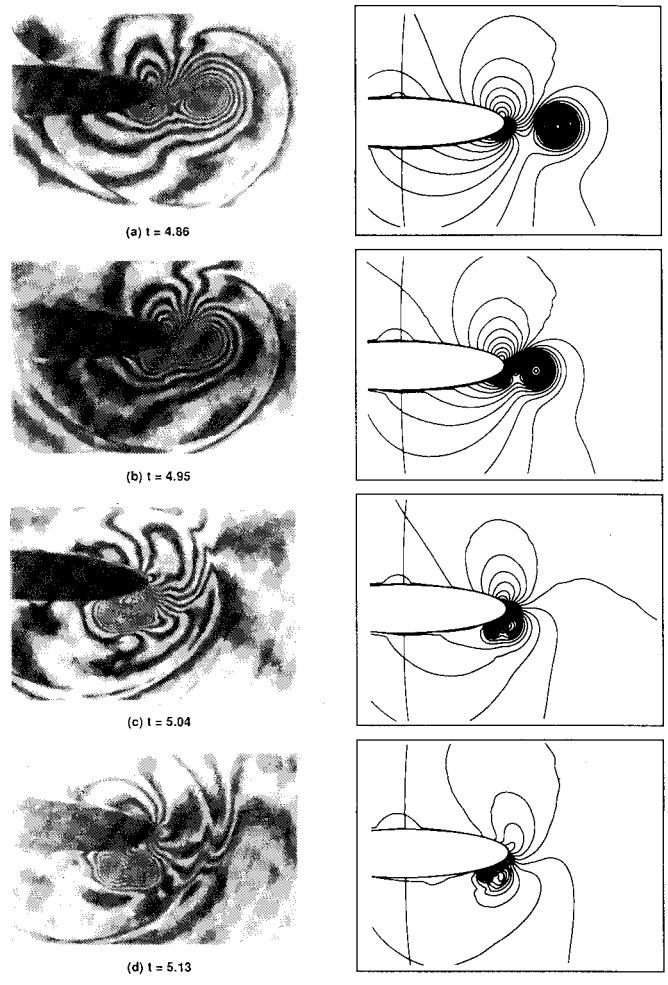

Fig. 13 Comparison of experimental holographic interferograms and computational snapshots during the head-on collision at $M_\infty = 0.5$, $\hat{\Gamma} = -0.283$, and $a_0 = 0.018$: lines in computation represent density contours; the holograms were taken at 25-μs intervals.

where the density ρ is obtained from

$$\frac{\gamma p/\rho}{\gamma - 1} + \frac{v_\theta^2}{2} = \frac{\gamma p_\infty/\rho_\infty}{\gamma - 1} \tag{11}$$

Equation (10) is integrated in conjunction with Eq. (11) using a Runge-Kutta scheme. The differential equation is integrated from a large value of r, where the pressure and density are known, along an inward direction toward the center of the vortex. Equations (9-11) represent a stationary vortex which satisfies the steady Euler equations. The Navier-Stokes equations, with appropriate boundary conditions, are first solved for steady-state solutions, then the vortex is initialized at the distance of 5 chord lengths ahead of the airfoil. The convection of the vortex and the interaction with the airfoil are then monitored.

Results and Discussion

Generation of Single Vortex

Figure 7 displays eight successive holographic interferograms, showing the generation of a shock-induced starting vortex and the convection of this vortex to the target airfoil. The holograms were taken at time increments of about 25 μs between exposures. At stage 1, typical triple-shock configurations are shown on both the upper and lower surfaces of the vortex generator. The shock front has passed the entire airfoil and the Mach stem is about to diffract around the trailing edge. A reflected shock and sliplines are clearly shown in this picture. At stage 2, the diffracted Mach stem from the lower surface intersects the Mach stem on the upper surface, and an attached vortex is formed. Mach-shock configurations exhibit conical similarity in terms of distance/time as time increases. At stage 3, the shock-induced starting vortex has detached and is beginning to move downstream. The starting vortex appears to have been knocked off the trailing edge by the advancing leeward-side shock. Although the vortex is detached, a residual connection to the trailing edge can be observed in the form of a periodic-structured layer with smaller scale vorticity. After stage 4, the vortex is convecting with the freestream induced by the shock. In these holograms, the shock becomes almost planar and sliplines are shown between the shock and the vortex.

Vortex Structure

To understand the physics of the BVI phenomenon, it is very desirable to know the precise structure of the vortex coming toward the airfoil. The vortex was generated by an NACA 0018 airfoil inclined by 30 deg. The convection velocity of the vortex was about 180 m/s ($M_\infty = 0.5$), which was measured by both holographic interferometry and three pressure transducers installed along the path of the vortex. Figures 8 and 9 show the holographic interferogram and its density distribution, respectively. The measured pressure distribution and its curve fit are shown in Fig. 10. In Fig. 11, the tangential velocity profile of the vortex, calculated from the curve fits of these two independent measurements, are compared with the analytical vortex model of Eq. (9). In this comparison, the experimental vortex has almost the same profile as the viscous

vortex model with $\hat{\Gamma} = -0.283$ and $a_0 = 0.018$. The core size of the vortex is much smaller than wing-tip trailing vortices which are typically 5 ~ 15% of the chord length.

Nielsen and Schwind,[14] following the work of Hoffman and Joubert,[15] divided the vortex into four distinct regions based on an analogy with the turbulent boundary layer: 1) a viscous core that is governed by viscous diffusion, 2) a logarithmic region that is dominated by turbulent diffusion, 3) a transition region to the outer inviscid region, and 4) an irrotational region in which the circulation is constant. Figure 12 shows the normalized circulation distribution of the experimental vortex with respect to r/a_0, where r is the distance from the center of the vortex and a_0 is the core size. The result is qualitatively very similar to the measurements of Tung et al.[16] on rotor-tip vortices using hot-wire anemometry, even though the present results are for a starting vortex. The proportionality constant in the linear region of the plot, which is dominated by turbulent diffusion, is given by 0.43 and is close to an average value of 0.39 reported by Tung et al., 0.44 by Corsiglia et al.,[17] 0.5 by Hoffman and Joubert,[15] and 0.5 by Phillips.[18] The curve-fit results are as follows.

Core region:

$$\Gamma/\Gamma_{max} = 0.80\,(r/a_0)^2, \qquad 0 \le r/a_0 < 0.62$$

Logarithmic region:

$$\Gamma/\Gamma_{max} = 0.51 + 0.43\,\ell n(r/a_0), \qquad 0.62 \le r/a_0 \le 1.8$$

Transition region:

$$\Gamma/\Gamma_{max} = 1 - 0.80\exp[-0.65(r/a_0)], \qquad 1.8 < r/a_0$$

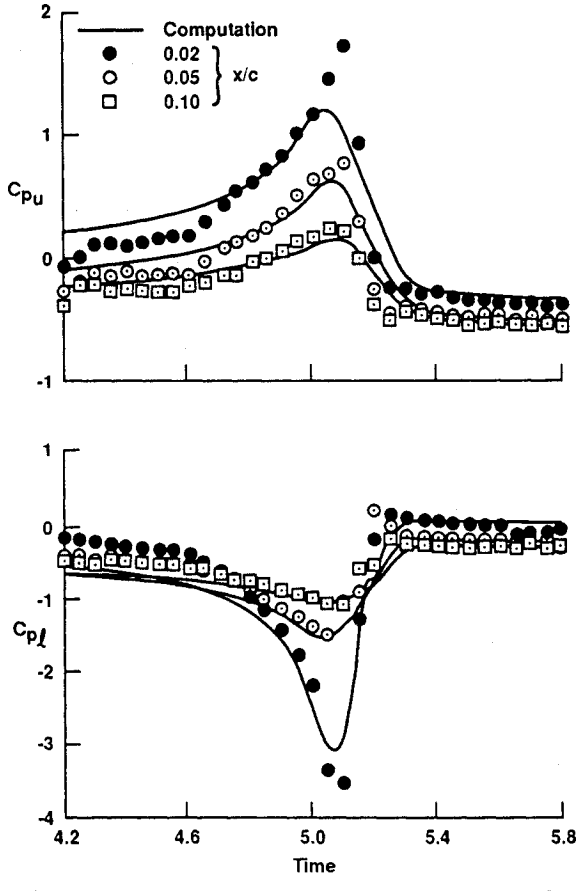

Fig. 14 Comparison of experimental and computational pressure histories at points near the leading edge during head-on BVI at $M_\infty = 0.5$, $\hat{\Gamma} = -0.28$, and $a_0 = 0.018$.

Head-On Collisional Blade-Vortex Interaction and Sound Wave Generation

Among all of the parallel BVIs, a head-on collision most strongly affects the aerodynamics near the leading edge and the resulting sound radiation because it has the largest interacting area. Figure 13 shows the comparison between the holograms and computational snapshots for the head-on collision case of $M_\infty = 0.5$, $\hat{\Gamma} = -0.283$, and $a_0 = 0.018$. In these interferograms, the freestream moves from right to left, opposite to the computation. In the first interferogram, a negative vortex (defined as a clockwise vortex in the left-to-right freestream) is moving toward the airfoil. As the vortex approaches the airfoil, there is a downward component of the velocity across the airfoil nose. This induced velocity makes the stagnation point move upward and causes the flow to separate on the lower surface. In the second hologram, the separation bubble grows and begins to convect with the flow. This secondary vortex is positive, different from the original one. In the third and fourth holograms, the stagnation point is moving back to its original position as the two vortices move downstream. The strength of each vortex is becoming weaker as they mix with each other. It is quite evident that the combination of the vortex weakening and their detachment from the airfoil surface means that such vortices have essentially no significant effect on the flow over the aft part of the airfoil. It also implies that the leading-edge radius is a more important reference parameter than the chord length when scaling the size of the vortex.

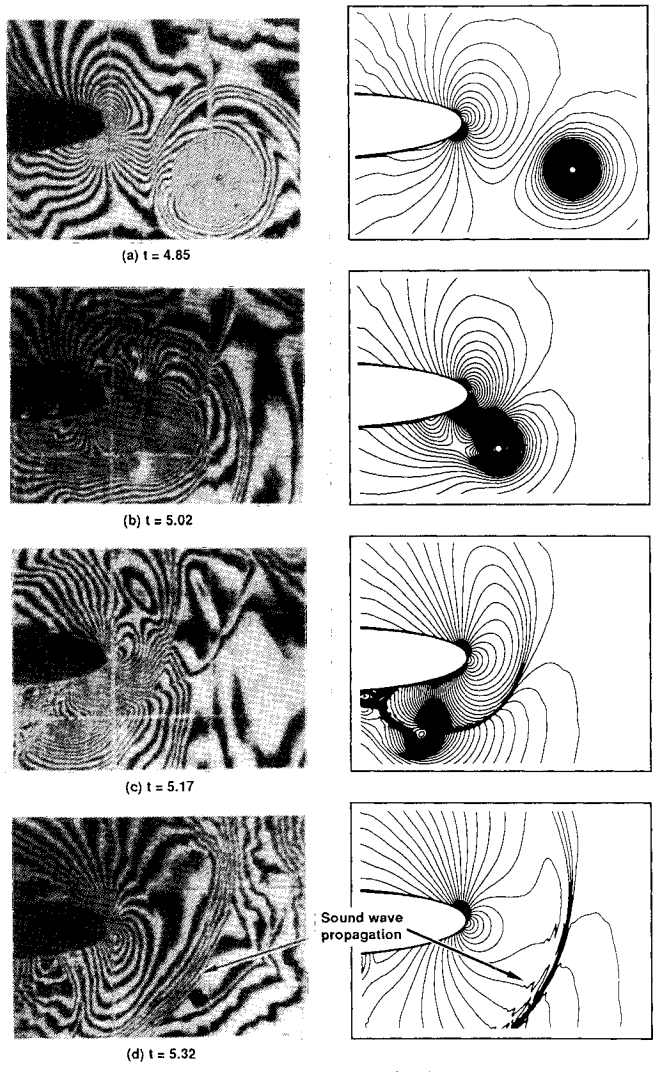

Fig. 15 Comparison of experimental holographic interferograms and computational snapshots during the head-on collision at $M_\infty = 0.7$, $\hat{\Gamma} = -0.37$, $a_0 = 0.024$, and $y_v = -0.1$.

In the computation, we also see the generation of secondary vortices due to flow separation and the oscillation of the stagnation point during the head-on BVI. The computational snapshots are very similar to the experimental pictures qualitatively, but the quantitative match is not exact. In Fig. 14, experimental pressure traces are shown at three selected positions (2, 5, and 10% of the chord length) and are compared with the computational results. Even though the two results are not perfectly matched, they are qualitatively very similar. The experimental traces show steeper slopes than those computed, and computed results underestimate the amplitudes of fluctuation. Another comparison between the density contours from interferograms and the computational snapshots is shown in Fig. 15. The conditions are $M_\infty = 0.7$, $\hat{\Gamma} = -0.37$, $a_0 = 0.024$, $y_v = -0.1$, and $\alpha = 3$ deg. The aerodynamic features in this case are almost the same as those shown in Fig. 15. The consecutive interferograms in this figure show the generation and propagation of a sound wave very clearly since the resolution of holograms is enhanced by an increase of the freestream density. In the second interferogram, opposing pressure peaks (high pressure on the upper side and low pressure on the lower side) are shown around the nose of the airfoil, which can be thought as an acoustic dipole. As the high-pressure region begins to relax to the low-pressure region, a sound wave radiates away from the airfoil. In computations reveal the same features and in overall sense are well-matched with the experimental results.

Conclusions

The results in this study indicate the following.

1) A highly two-dimensional, shock-induced starting vortex can be generated in a shock-tube.

2) The tangential velocity profile of a convecting vortex can be calculated from measurements independently obtained of the density and pressure distributions of the vortex. A set of empirical formula was found for a two-dimensional compressible, viscous vortex.

3) Holographic interferograms show the formation of opposite pressure peaks near the leading edge of the airfoil and the propagation of a sound wave in a head-on BVI, which are also predicted by the Navier-Stokes simulation.

4) In both the experiment and the computation, flow separation on the lower leading edge is shown, which implies that viscosity plays a significant role in that case of a strong BVI.

5) Surface pressure measurements during a head-on BVI indicate that the Navier-Stokes simulation underpredicts the effect of the interaction even though a large number of grid points and a high-order scheme are used.

Acknowledgments

This work was sponsored by NASA Ames Research Center and the U.S. Army Research Office under Contract NCA2-339. The authors wish to thank M. M. Rai for providing his BLADE code and special comments. Useful comments of C. Tung, Y. H. Yu, and K. W. McAlister are also gratefully acknowledged.

References

[1]Schmitz, F. H., and Boxwell, D. A., "In-Flight Far Field Measurement of Helicopter Impulsive Noise," *Journal of American Helicopter Society,* Vol. 21, No. 4, 1976, pp. 2–16.

[2]Tangler, J. L., "Schlieren and Noise Studies of Rotors in Forward Flight," 33rd Annual National Forum of the American Helicopter Society, Paper 77, 33-05, Washington, DC, May 1977.

[3]Nakamura, Y., "Prediction of Blade-Vortex Interaction Noise from Measured Blade Pressure," Seventh European Rotorcraft and Powered Lift Aircraft Forum, Paper 32, Garmisch-Partenkirchen, Germany, 1981.

[4]Caradonna, F. X., Strawn, R. C., and Bridgeman, J. O., "An Experimental and Computational Study of Rotor-Vortex Interactions," *Vertica,* Vol. 12, No. 4, 1988.

[5]Straus, J., Renzoni, P., and Mayle, R. E., "Airfoil Pressure Measurements During a Blade-Vortex Interaction and a Comparison with Theory," AIAA Paper 88-0669, Jan. 1988.

[6]Meier, G. E. A., and Obermeier, F., "Noise Generation and Boundary Layer Effects in Vortex-Airfoil Interaction and Methods of Digital Hologram Analysis for These Flow Fields," Final Tech. Rept., European Research Office of the U.S. Army, London, Sept. 1990, pp. 1353–1359.

[7]Bershader, D., "Foundation of the Blade-Vortex Interaction Problem: Structure and Behavior of Trailing Compressible Vortices," Summary Rept. to U.S. Army Research Office, Stanford Univ., Stanford, CA, 1988.

[8]Booth, E. R., Jr., "Experimental Observation of Two-Dimensional Blade-Vortex Interaction," *AIAA Journal,* Vol. 28, No. 8, 1990, pp. 1353–1359.

[9]Rai, M. M., and Chakravarthy, S. R., "An Implicit Form for the Osher Upwind Scheme," *AIAA Journal,* Vol. 24, No. 5, 1986, pp. 735–743.

[10]Rai, M. M., "Navier-Stokes Simulation of Blade-Vortex Interaction using High Order Accurate Upwind Schemes," AIAA Paper 87-0543, Jan. 1987.

[11]Rai, M. M., and Chaussee, D. S., "New Implicit Boundary Procedures: Theory and Application," *AIAA Journal,* Vol. 22, No. 8, 1984, pp. 1094–1100.

[12]Rai, M. M., "Navier-Stokes Simulations of Rotor-Stator Interaction Using Patched and Overlaid Grids," AIAA Paper 85-1519, July 1985.

[13]Sculley, M. P., "Computation of Helicopter Rotor Wake Geometry and Its Influence on Rotor Harmonic Loads," Massachusetts Inst. of Technology, ASRL TR-178-1, Boston, MA, 1975.

[14]Nielsen, J. N., and Schwind, R. G., "Decay of a Vortex Pair behind an Aircraft," *Aircraft Wake Turbulence and its Detection,* edited by J. Olson, A. Goldberg, and M. Roger, Plenum, New York, 1971, pp. 413–454.

[15]Hoffman, E. R., and Joubert, P. N., "Turbulent Line Vortices," *Journal of Fluid Mechanics,* Vol. 16, Pt. 3, 1963, pp. 395–411.

[16]Tung, C., Pucci, S. L., Caradonna, F. X., and Morse, H. A., "The Structure of Trailing Vortices Generated by Model Rotor Blades," *Vertica,* Vol. 7, No. 1, 1983, pp. 33–43.

[17]Corsiglia, V. R., Schwind, R. G., and Chigier, N. A., "Rapid Scanning, Three-Dimensional Hot Wire Anemometer Surveys of Wing Tip Vortices," *Journal of Aircraft,* Vol. 10, No. 12, 1973, pp. 752–757.

[18]Phillips, W. R. C., "The Turbulent Trailing Vortex during Roll-Up," *Journal of Fluid Mechanics,* Vol. 105, 1981, pp. 451–467.